

Relativistic Leaky Surface Plasmon Accelerator in Nanostructured Carbon Nanotube Forest

Bifeng Lei,^{1,2,*} Hao Zhang,^{1,2} Cristian Bonțoiu,^{1,2} Alexandre Bonatto,³ Pablo Martín-Luna,⁴ Bin Liu,⁵ Javier Resta-López,⁶ Guoxing Xia,^{7,2} and Carsten Welsch^{1,2}

¹*Department of Physics, The University of Liverpool, Liverpool, L69 3BX, United Kingdom*

²*Cockcroft Institute, Warrington WA4 4AD, United Kingdom*

³*Federal University of Health Sciences of Porto Alegre, Porto Alegre, RS, 90050-170, Brazil*

⁴*Instituto de Física Corpuscular (IFIC), Universitat de València -*

Consejo Superior de Investigaciones Científicas, 46980 Paterna, Spain

⁵*Guangdong Institute of Laser Plasma Accelerator Technology, Guangzhou, China*

⁶*ICMUV, Universidad de Valencia, 46071 Valencia, Spain*

⁷*Department of Physics and Astronomy, The University of Manchester, Manchester M13 9PL, United Kingdom*

(Dated: February 20, 2025)

In quantum-degenerate metallic carbon nanotubes (CNTs), the conduction electron gas forms a solid-state plasma environment where collective dynamics are dominant. This dense plasma is capable of supporting the excitation of surface plasmon on the CNT surface. In this study, we demonstrate a new class of microscale relativistic surface plasmons (RSPs) that, independent of laser polarisation and matching medium, can be directly excited by paraxial propagation of a high-intensity optical laser pulse through a cylindrical vacuum channel nanostructured in a CNT forest. The leaky field of the resonant RSP mode can support a non-evanescent longitudinal component with amplitude up to several TV/m-levels and a phase-matched focusing field. This field enables the sustained acceleration of relativistic electrons and positrons over long distances. We also investigate two possible mechanisms for electron injection, including edge injection and self-injection, both of which are feasible with current laser facilities, paving the way for experimental realisation. As well as highlighting a promising avenue for the development of ultra-compact, high-energy solid-state plasma particle accelerators, this work also opens up the potential for high-energy plasmonics.

I. INTRODUCTION

Plasmon is a quantum quasi-particle that represents the self-sustained collective oscillation of degenerate electrons in conductive materials, such as metals and semiconductors, driven by the long-range Coulomb interactions between conduction electrons. Plasmons can be excited by external sources, such as photons or charged particle beams [1, 2]. Within the bulk of plasma, this excitation is referred to as a bulk plasmon, characterised by the quantum energy $\hbar\omega_p$, where \hbar is the reduced Planck's constant and ω_p is the plasmon frequency, given by $\omega_p = \sqrt{4\pi e^2 n_e / m_e}$ with n_e the ambient plasma electron density and m_e the rest electron mass. Plasmons can also be excited at the interface between a metal and a surrounding medium, forming surface plasmons (SPs). These SPs propagate along the interface with a phase velocity determined by the driving source. They exhibit unique eigenfrequencies and polarisation fields that depend on the surface geometry. The strongest excitation of SPs occurs at the resonance frequency, which for a perfectly flat metal surface is $\omega_r = \omega_p / \sqrt{1 + \epsilon}$ [3–5], where ϵ is the dielectric constant of the bounding medium. For a vacuum boundary, where $\epsilon = 1$, this simplifies to $\omega_r = \omega_p / \sqrt{2}$ [6]. SPs are of particular interest due to their ability to propagate over significant distances along

the surface while maintaining strong field confinement in a narrow region near the boundary, enabling applications in fundamental physics [7, 8], electrochemistry [9], biosensing [10], plasmonic chip technology [11], and advanced microscopy [12, 13].

The confined strong electromagnetic (EM) fields of SPs are suitable for particle acceleration [14, 15]. In the non-relativistic plasmonic schemes, low-intensity laser pulses ($I < 10^{18}$ W/cm²) interact with sub-wavelength nanostructured targets, such as gratings, to generate strong localised fields [16, 17]. In the high-field regime driven by high-intensity laser pulses, the dynamics of plasma electrons and the behaviour of SPs become nonlinear and relativistic [18, 19]. These relativistic surface plasmons (RSPs) can sustain significantly higher field strengths than that of non-relativistic SPs and thus provides new opportunities for manipulating intense light and particle beams. For example, RSP excitation on solid targets has been shown to enhance the acceleration of protons [20] and electrons [21–23], and it plays a pivotal role in high-order surface harmonic generation [18, 24]. Recent advances in nanostructured materials [25–28] have aroused significant interest in using RSPs for high-energy particle acceleration [29–32]. However, the EM field of RSPs on planar surfaces decays exponentially in the normal direction, limiting their effective range and posing challenges for efficient relativistic particle acceleration. Moreover, significant challenges remain in the electrical, thermodynamic and mechanical properties of conventional metals used in these applications. Exciting RSPs on conven-

* bifeng.lei@liverpool.ac.uk

tional metal surfaces presents several challenges under strong field conditions. Traditional plasmonic metals often cannot withstand high-intensity fields without degradation. Significant ohmic (resistive) losses result in rapid attenuation of surface plasmon waves, while excessive heating can alter the metal's properties, induce structural damage, and compromise the stability of plasmonic modes. Additionally, nonlinear optical effects in metals, such as harmonic generation and self-phase modulation, can further complicate the control and predictability of plasmonic excitations. Addressing these limitations is critical to fully realising the potential of RSP-based systems in high-energy and high-field applications.

Carbon nanotubes (CNTs) are graphene-based synthetic nanostructures formed by rolling single or multiple graphene sheets into cylindrical shapes. With inner diameters typically spanning a few nanometers and lengths extending up to millimetres, CNTs exhibit exceptional mechanical, thermodynamic, and electronic properties [33, 34]. Depending on their chirality, CNTs can behave as metallic conductors (armchair type) and act as polarisable media in a quantum-degenerate state [35, 36]. In this state, external sources, such as laser fields, can displace conduction electrons, creating electric dipoles through ponderomotive scattering. This displacement enables the excitation of SPs on the CNT surface [37]. Each carbon atom contributes approximately one conduction electron due to sp^2 hybridisation, leading to an electron number density up to the order of 10^{24} cm^{-3} in individual CNTs. Unlike traditional metals, CNTs exhibit collisionless electron transport due to their unique structural, electronic, and quantum properties. This allows electrons to transport micrometre (μm)-scale distances without significant energy loss [38, 39]. The resulting dense electron plasma can theoretically support extremely high acceleration gradients, reaching several TV/m. The hollow, vacuum-like channels within CNTs enable photon or particle beams to propagate over extended distances, generating wakefields for particle acceleration when driven by short, high-density particle beams [40] or X-ray laser pulses [27]. However, a single CNT currently cannot support efficient particle acceleration due to the mismatch between the μm -scale dimensions of available photon or particle beams and the natural nanoscale dimensions of CNTs. As a result, direct experimental demonstrations are still lacking, as achieving resonant coupling between CNT structures and high-energy beams remains a challenge.

A nanostructured CNT forest is an organised array of vertically aligned carbon nanotubes, resembling a dense forest [41, 42]. For instance, Fig.1 illustrates a porous configuration of such a forest where a μm -scale central vacuum channel allows the stable propagation of an optical laser pulse. These structures are typically synthesised using advanced techniques like chemical vapour deposition (CVD) [43, 44]. Unlike unstructured solids, CNT forests offer significant flexibility in terms of geometry, density, and surface structure [45–47]. The density of

a CNT forest can be precisely controlled by adjusting parameters such as the packing density or the volume fraction of CNTs [48], achieving typical densities in the range of $n_e \sim 10^{19-23} \text{ cm}^{-3}$. This density flexibility provides the RSPs excitation with exceptional tunability. For example, the characteristics of RSPs can be adjusted to exhibit predominantly electrostatic or electromagnetic behaviour [49], thereby enabling precise control over light-CNT interactions and optimised performance in high-field plasmonic and photonic applications. The dense plasma within the solid-state CNT forest supports ultra-high acceleration gradients, ranging from hundreds of GV/m to tens of TV/m, while also providing a structurally robust medium for particle acceleration compared to traditional gaseous plasmas.

In this paper, we demonstrate that independent of laser polarisation or the matching medium, RSPs can be directly excited by a TW laser pulse and effectively confined over a sufficiently long distance along the cylindrical surface of a quantum-degenerate CNT forest. The longitudinal component of the resulting leaky field is μm -scale, non-evanescent. Due to the relativistic effect, it has a phase velocity close to the speed of light. Its amplitude can reach up to TV/m-level, enabling highly efficient acceleration of relativistic electrons and positrons over hundreds of μm , supported by a strong, phase-matched transverse focusing field. We introduce two electron injection mechanisms: edge injection and self-injection. In edge injection, a well-defined electron beam with a narrow energy spectrum, sub- μm beam size, fs duration, and pC charge is trapped during the laser pulse entering the forest channel. In contrast, self-injection is a continuous process in which the emission of wall electrons into the central vacuum region leads to the self-trapping of an electron beam with a broader energy spectrum and nC charge. Additionally, we provide a theoretical analysis of the fundamental physical mechanisms behind leaky RSP excitation and evaluate the experimental feasibility. This work offers valuable insights into advanced particle acceleration and presents promising applications for high-energy plasmonics and photonics.

II. RELATIVISTIC SURFACE PLASMON AND LEAKY FIELD IN THE NANOSTRUCTURED CNT FOREST

Direct excitation of SPs at a flat interface is generally impossible due to the momentum mismatch between the incident EM wave and the SP mode, except in leaky mode configurations [50]. Here, we can show that the RSPs can be directly excited on a surface of low electron density $n_e < n_c$ by a high-intensity laser pulse, where $n_c = m_e \omega_L^2 / 4\pi e^2$ is the critical density of the laser pulse. $\omega_L = 2\pi/\lambda_L$ is the laser frequency and λ_L is the laser wavelength. The field energy is not fully confined to the surface but can leak into the vacuum region. However, the resulting leaky field is evanescent on a flat surface,

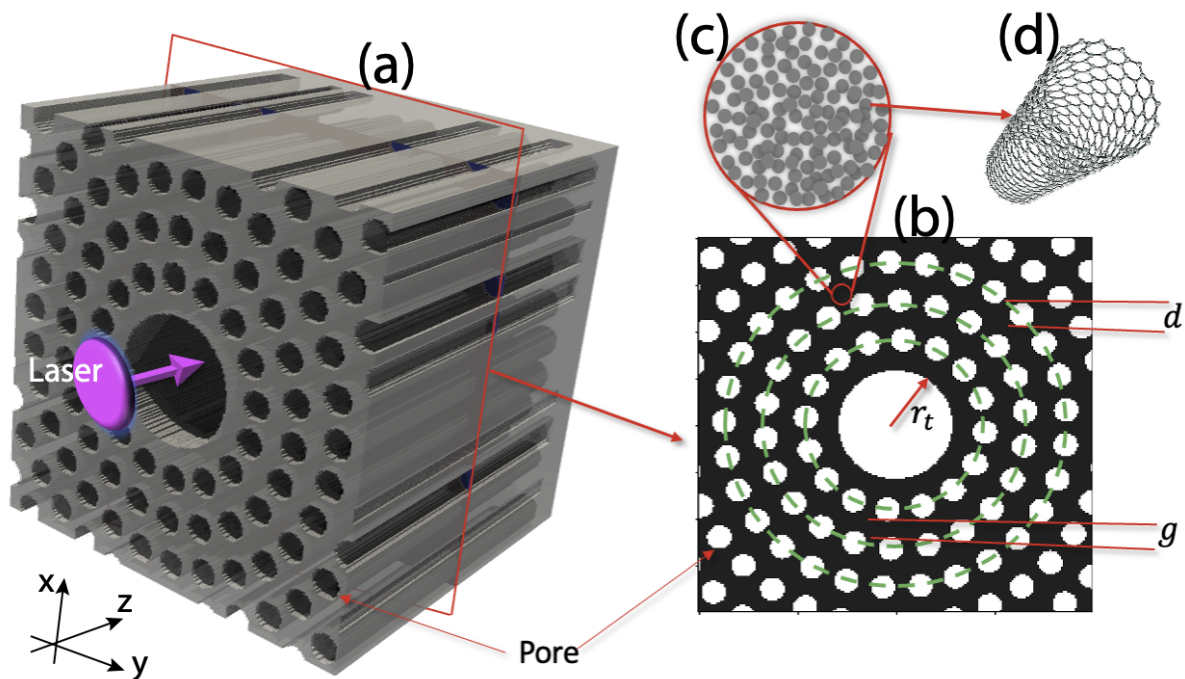


Figure 1. Schematic representation of (a) a nanostructured CNT forest target in a porous configuration and (b) its transverse layout, showing key parameters such as pore diameter d , central channel radius r_t , and virtual layer gap g . (c) A zoomed-in view of the transverse structure of the CNT forest, where each grey dot represents an individual single-wall or multi-wall CNT, as further detailed in (d). The laser pulse (represented by the pink spot in (a)) propagates along the central channel in the z direction.

limiting its suitability for relativistic particle acceleration, as discussed in Sec. IV B. In contrast, a nanostructured CNT forest, with its cylindrical surface geometry, can significantly modify the spatial and temporal characteristics of the leaky field, as shown in Fig. 2.

We consider a 5 TW optical laser pulse of wavelength $\lambda_L = 0.8 \mu\text{m}$ passing through the vacuum channel of a nanostructured CNT forest target arranged in a porous pattern as seen in Fig. 1. The target is designed with a cylindrical vacuum channel of radius $r_t = 3.0 \mu\text{m}$. Details of the target configuration are summarised in Table 2 and discussed in Sec. IV D. The laser pulse is linearly polarised in the y direction and propagates in the z direction. It is focused at the entrance of the channel $z = 0 \mu\text{m}$ with root-mean-square (RMS) waist $w_0 = 3.0 \mu\text{m}$ and duration $\sigma_\tau = 6.0 \text{ fs}$. These parameters give a normalised laser strength $a_0 = 4.0$ or intensity $I = 3.4 \times 10^{19} \text{ W/cm}^2$, with the field intensity of $1.46 \times 10^{19} \text{ W/cm}^2$ on the inner surface of the vacuum channel which drives the relativistic electron dynamics. The fully 3D simulations were conducted using the particle-in-cell (PIC) code WarpX [51].

The wall electrons oscillate collectively driven by the ponderomotive scattering and are confined to the surface due to the transverse ionic potential, as shown in Fig. 2(a), where the laser pulse has propagated $60 \mu\text{m}$ within the forest channel. A microscale monochromatic leaky field inside the vacuum channel is excited at the relativistic resonant frequency, $\omega_R = \omega_p / \sqrt{2\gamma_e}$

and γ_e the Lorentz factor of wall electron. The wavelength obtained from PIC, $\lambda_{R,\text{PIC}} = 5.0 \mu\text{m}$, agrees well with the theoretical prediction with relativistic effect, $\lambda_{R,\text{Theo.}} = 2\pi c / \omega_R = 4.8 \mu\text{m}$, as discussed in Sec. IV B. In comparison, the non-relativistic prediction is $\lambda_{r,\text{Theo.}} = 2\pi c / \omega_r = 3.3 \mu\text{m}$ [4]. The energy of RSP is $\hbar\omega_R = 0.24 \text{ eV} \gg E_F = 0.05 \text{ eV}$, where $E_F = \hbar^2(3\pi^2 n_e)^{2/3} / 2m_e$ is the Fermi energy. This indicates that Landau damping does not occur [52]. On the other side, as the RSP energy is slightly higher than that of optical phonon in typical CNTs in the range of $0.15 - 0.2 \text{ eV}$ [53], the optical damping effect can also be neglected. As a result, a long propagation distance of RSP is possible. For example sub-mm distance has been seen from PIC simulations. The longitudinal component of the leaky field remains quasi-uniform across the vacuum channel with an amplitude of 0.2 TV/m , providing periodic accelerating phases for both negatively and positively charged particles, as shown in Fig. 2 (a), (c), and (d), which is advantageous for maintaining beam quality. The transverse component of the field, $W_x = E_x - cB_y$, supplies a focusing force for positrons, phase-matched with the corresponding acceleration phase, as shown in Fig. 2(b) and by the black line in (e). This field reaches an amplitude of 0.3 TV/m on the surface and decays transversely. In the phase for electron acceleration, the transverse field vanishes in the vacuum region, instead providing a confining force on the inner surface, as shown

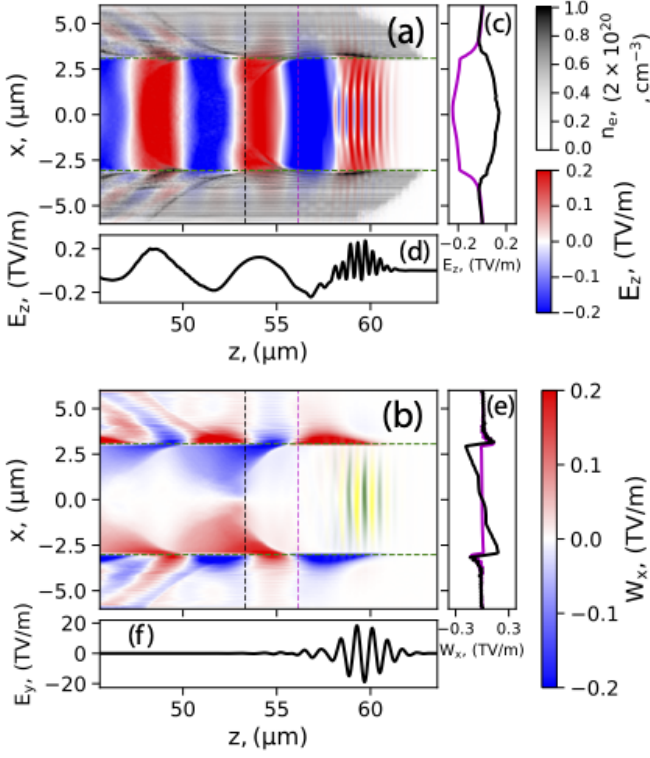


Figure 2. PIC results after laser pulse propagating $z = 60 \mu\text{m}$ inside the CNT forest channel: (a) Conduction electron density distribution n_e (grey colourmap), longitudinal acceleration field E_z (blue-red colourmap) in xz -plane sliced at $y = 0 \mu\text{m}$. (b) Transverse field $W_x = E_x - cB_y$ in xz -plane sliced at $y = 0 \mu\text{m}$. The green-yellow colourmap shows the laser field. (c) Transverse slice of E_z along the dashed pink and black lines in (a), respectively. (d) On-axis ($x = 0 \mu\text{m}$) plot of E_z . (e) Transverse slice of W_x along the dashed pink and black lines in (b), respectively. (f) On-axis ($x = 0 \mu\text{m}$) plot of E_y . The horizontal green dashed lines in (a) and (b) indicate the positions of the inner surface of the forest.

by the green line in Fig. 2(e). Consequently, electrons can also be confined within the vacuum channel and accelerated. The laser pulse propagates through the vacuum channel without any noticeable deformation, as shown in Fig. 2 (b) and (f). This demonstrates that the scheme is dynamically stable and can be effectively scaled for long porous targets, limited only by the depletion of the laser energy.

In order to be successfully accelerated, a relativistic electron or positron beam should be injected into the correct phase. We now put either an electron or positron beam in the corresponding accelerating phase, indicated by vertical dashed pink and black lines in Fig. 2(a) and (b), respectively. Both of the beams have the same parameters except for the negative or positive charge, as summarised in Table.1.

The evolution of energy gain and transverse beam size is shown in Fig. 3 (a) and (b), respectively. All the electrons and positrons inside the witness beam can be pre-

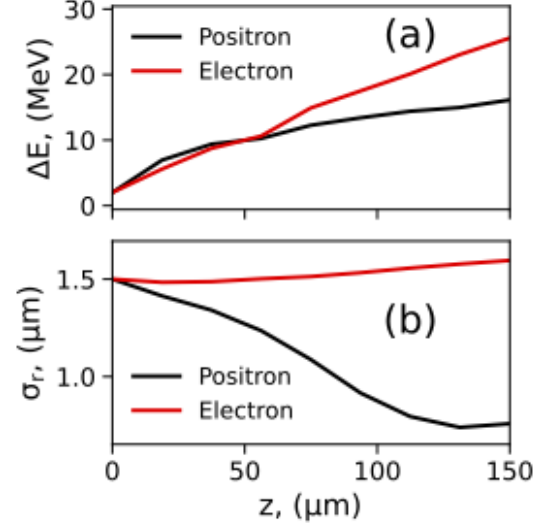


Figure 3. PIC Results: (a) Evolution of the energy gain of witness positron (black) and electron (red) beams at the acceleration phase indicated by the vertical dashed lines in Fig. 2(a). (b) Evolution of radial beam size $\sigma_r = \sqrt{\sigma_x^2 + \sigma_y^2}$, where $\sigma_{x,y}$ denotes the transverse RMS sizes of witness positron (black) and electron (red) beams in x and y directions, respectively.

Table 1. Parameters of the witness positron and electron beams used in simulations.

Beam profile	Gaussian
Charge, Q_{e^+,e^-}	± 1 pC
Beam energy, \mathcal{E}	200 MeV
Beam RMS size, σ_r	1.5 μm
Beam RMS duration, σ_τ	1.6 fs
Energy spread	1.0%

served and accelerated which indicates that the transverse component of the RSPs on the inner surface can sufficiently confine both beams. With the positron beam, after $z = 150 \mu\text{m}$ propagation, the beam gains energy $\Delta E = 19$ MeV energy which indicates the mean energy gain rate as $R_E = 0.12$ TeV/m. The beam size is reduced by half due to the strong transversely leaky field and is then equilibrated at $z = 130 \mu\text{m}$, where the focusing field of RSP is in balance with the self space-charge field of the witness beam. For the witness electron beam, the energy gain is $\Delta E = 25$ MeV, which indicates the mean energy gain rate as $R_E = 0.16$ TeV/m. The radial beam size is preserved with a small increase as the transverse component of the leaky field at the acceleration phase for the electron beam is weaker than that for the positron beam as shown in Fig. 2(b) and (e). Additionally, the quasi-linear energy gain indicates that the phase slippage between the witness beam and leaky field is slow and then enables the extensible acceleration for high-power laser pulse as discussed in Sec. IV C.

III. ELECTRONS INJECTION

In experiments, a positron beam must be externally injected into the appropriate phase of the leaky field to achieve acceleration, as the CNT target does not inherently generate positrons. Currently, available positron sources can produce positron beams with energies at the MeV-level, making this approach feasible [54].

For electron acceleration, it is more feasible that the wall electrons can be self-injected into the correct phase of the leaky field if these electrons can meet three criteria: firstly, they must be emitted freely from the inner surface into the vacuum channel; secondly, they must be relativistic to catch up with the phase velocity of the leaky field; and thirdly, they must be confined within the channel. The first condition is crucial, which requires the wall electrons to attain a sufficient transverse momentum to overcome the confinement on the surface. Here, we show two possible mechanisms that could efficiently inject the wall electrons into the correct phase for acceleration.

A. Edge injection

With a low-intensity laser pulse, wall electrons gain relatively low momentum and are unable to overcome the two-dimensional (2D) transverse confinement on the channel surface, preventing them from freely crossing the inner vacuum surface. However, the situation changes during the laser enters the forest channel. Here, the vertical edge provides an additional dimension of confinement in the longitudinal direction, which compresses the streaming electrons, as shown in Fig. 4. This compression allows some electrons to gain additional momentum which allows them to overcome the transverse confinement and emit into the vacuum channel. Since the RSPs are localised waves, the emitted electrons are naturally in the acceleration phase along the surface and are simultaneously accelerated longitudinally while drifting transversely through the vacuum channel. These electrons collide at the channel centre and become trapped in the leaky field once they acquire sufficient longitudinal momentum. This method is analogous to catapult injection at the edge of stacked graphene layers [55]. PIC simulations reveal that after 100 μm of propagation, a 42 pC electron beam with a duration of 3.3 fs is accelerated to 35 MeV with a 1% energy spread, corresponding to a mean acceleration gradient of 0.35 TeV/m. The beam transverse size is $\sigma_r = 0.2 \mu\text{m}$. Such an ultrashort, high-quality beam holds unprecedented potential for advanced applications in high-field science and beyond [56].

B. Self injection

With increased laser strength, electron oscillations on the surface intensify, leading to a significant enhancement of the RSP amplitude, as demonstrated in Fig.5(a),

where a laser pulse with $a_0 = 10$ or peak power $P = 30$ TW is used. This enhancement enables some wall electrons to gain sufficient transverse momentum to cross the inner surface and penetrate deeply into the vacuum region. These electrons naturally traverse the forest surface through the accelerating phase of the RSP and align with the accelerating phase of the leaky field in the vacuum channel. The leaky field, with a magnitude as high as 0.6 TV/m, facilitates the rapid longitudinal acceleration of these transiting electrons, allowing them to catch up with the leaky field within just a few μm . The transverse field of the RSP acts as a confining force along the inner surface, preventing the transited electrons from escaping back into the forest wall, as illustrated in Fig. 5(b). Here, the transverse component of the leaky field vanishes across most of the acceleration phase region, ensuring stability. As a result, a substantial number of electrons are trapped and continue to be efficiently accelerated.

A 204 pC electron beam is self-injected and accelerated to 35 MeV over an 80 μm long-distance, corresponding to a peak acceleration gradient of $G = 0.43$ TeV/m. The mean beam energy is 20.4 MeV, yielding a mean acceleration gradient of $G = 0.26$ TeV/m. The phase space and energy spectrum of the accelerated beam are presented in Fig.5(c) and (d), respectively, which show a broad spectrum. Electrons continuously transit across the inner surface until the laser pulse is sufficiently depleted, allowing the self-injection process to persist, as discussed in Sec.IV C. The high-energy component peaks at 30 MeV with a 26% spread, while the low-energy component peaks at 5.4 MeV with a 1% spread. This self-injection mechanism is fully feasible with currently available high-power laser facilities, offering a promising pathway for experimental demonstration of this proposed CNT forest-based plasma accelerator.

IV. DISCUSSION AND METHODS

A. Quantum degeneracy and correlation

The excitation of RSPs discussed in this paper relies on the collective dynamics of high-density conduction electrons which can be treated as a classical plasma if the CNT forest is in quantum degenerate state [1]. To establish the feasibility of this condition, we first examine how it can be satisfied under typical experimental conditions, ensuring the required electron density and temperature ranges are achievable within current experimental setups.

Metallic crystals such as CNTs exhibit quantum degeneracy at low temperatures or high carrier densities, a state governed by the Pauli exclusion principle [57, 58]. In this quantum degenerate state, the conduction electrons act as highly degenerate carriers, forming a Fermi gas that dictates the quantum behaviour of the fermions, such as minimum scattering. Electrons with energy near the Fermi level can move freely in response to small perturbations, such as electric fields, resulting in high electric

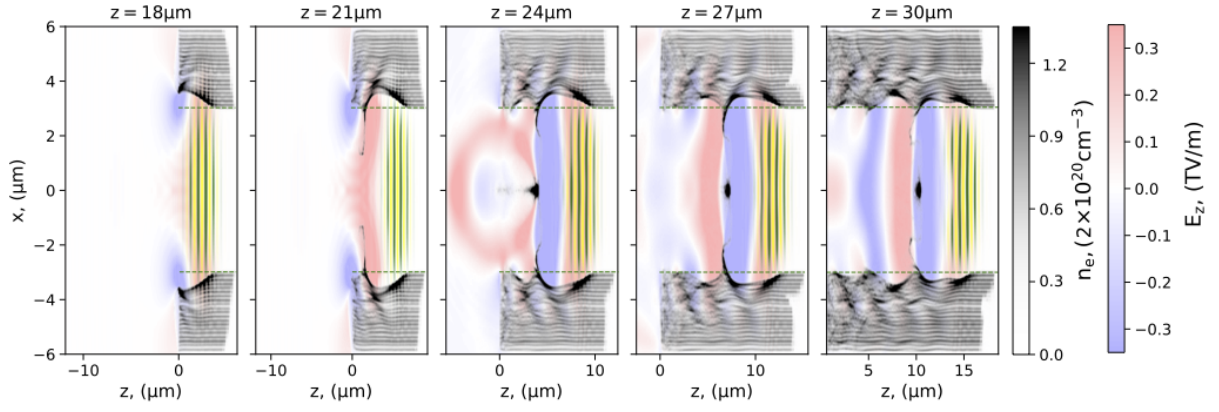


Figure 4. PIC results: Evolution of the electron density (grey colourmap), longitudinal electric field (blue-red colourmap), and laser field (green-yellow colourmap) at five propagation positions: $z = 18, 21, 24, 27$ and $30 \mu\text{m}$. The laser strength is $a_0 = 5.0$, with other parameters the same as those in Fig. 2. The horizontal green dashed lines indicate the positions of the inner surface of the forest.

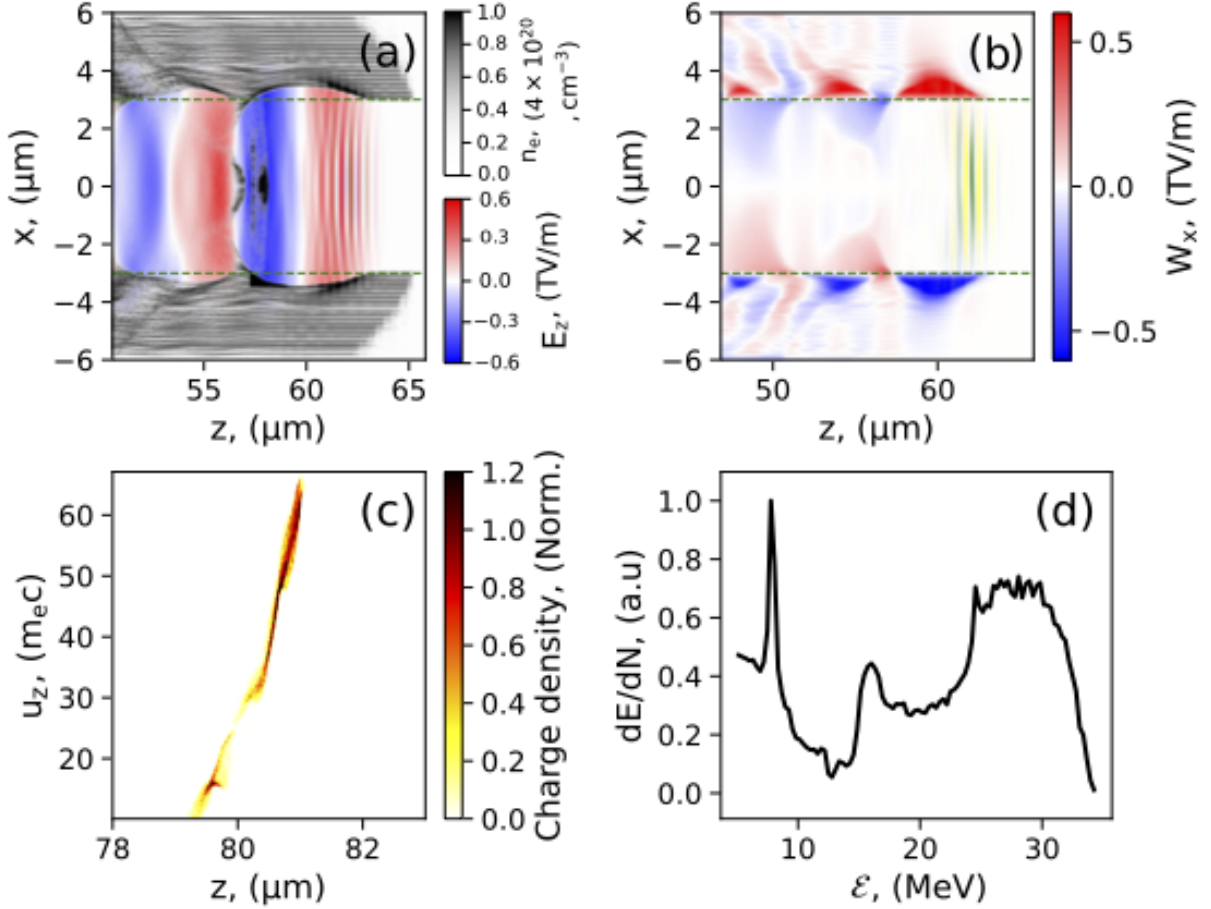


Figure 5. PIC results: (a) Electron density distribution (n_e , grey colourmap), and longitudinal electric field (E_z , blue-red colourmap). (b) Transverse field, W_x (blue-red colourmap) and laser field (yellow-green colourmap). (c) Phase space of the accelerated electron beam after exiting the $80 \mu\text{m}$ long forest target. (d) Energy spectrum corresponding to (c). All the laser and target parameters are the same as these used for Fig. 2 except the laser strength which is increased to $a_0 = 10$. The horizontal green dashed lines in (a) and (b) indicate the positions of the inner surface of the forest.

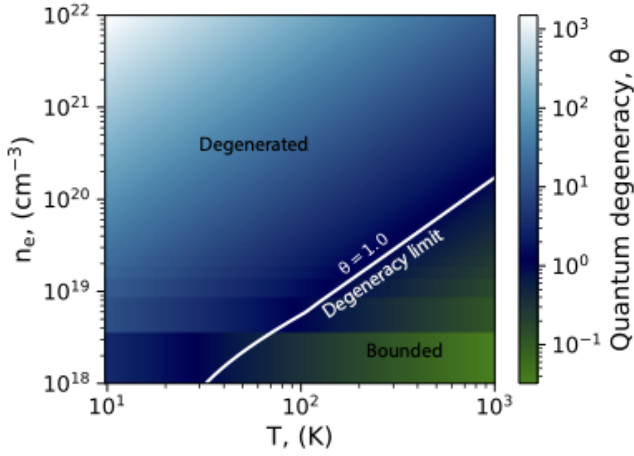


Figure 6. Quantum degeneracy parameter θ as a function of temperature T and electron density n_e .

cal conductivity and low thermal sensitivity. The quantum degeneracy parameter, θ , quantifies the extent to which a system is quantum degenerate and is defined by

$$\theta = \frac{E_F}{K_B T}. \quad (1)$$

K_B is the Boltzmann constant and T is the temperature. Quantum degeneracy requires $\theta \gg 1$, indicating that the Fermi energy is significantly larger than the thermal energy. In CNTs, the conduction electron density ranges from $10^{18} - 10^{24} \text{ cm}^{-3}$ and can support a degenerate Fermi electron gas over a wide parameter space (shown in Fig. 6). For example, with an electron density of $n_e = 2.0 \times 10^{20} \text{ cm}^{-3}$, quantum degeneracy is maintained at temperatures up to $T = 400 \text{ K}$. Therefore, under typical laboratory conditions, these conduction electrons form a collisionless dense plasma environment in which the positive background charge can be assumed to be uniformly distributed, creating a stabilising field. Furthermore, interactions between electrons and lattice vibrations and photons are often neglected. This validates the classical kinetic method for studying the RSP excitation in the CNT forest, as presented in this paper.

In an electron gas, particles interact strongly due to the long-range nature of the Coulomb force. When the electron density is sufficiently high, collective behaviour, such as plasmons, becomes dominant. In this regime, the dynamics of each electron do not depend individually on the other electrons but on a smeared potential created by the collective electron cloud. This correlated state of the electron gas leads to macroscopic quantum effects and collective behaviour [1]. To sustain collective behaviour, the damping time must exceed the average oscillation period of these collective modes, which is given by the ratio

$$\eta = \frac{\tau_{\text{damp}}}{\tau_{\text{coll}}} = \frac{\hbar/(2\pi K K_B T)}{2\pi/\omega_p}, \quad (2)$$

where τ_{damp} is the damping time of the degenerate electron gas and τ_{coll} is the period of the collective oscillations. Here K represents the Luttinger parameter, typically in the range of 0.2 to 0.5 for metallic CNTs [59]. Eq. (2) indicates that quantum correlations are also favoured under conditions of high electron density or low temperature. In the case of CNTs with typical parameters, the high value of $\eta \gg 1$ confirms the presence of significant quantum correlations in this system.

As a result, the conduction electron gas in CNTs can generally be approximated as a classical plasma in which electrons move freely in a quasi-uniform background. The dominant collective dynamics in this regime can be effectively studied using classical kinetic theory. Quantum effects such as plasma dispersion corrections, photon-electron coupling, polariton interactions and collision damping can be safely neglected due to their minimal influence under these conditions.

B. Leaky field of RSPs in flat and cylindrical geometry

A high-intensity laser pulse propagating along a plasma-vacuum boundary excites the confined surface waves which can be treated as the polarisation of the plasma in response to the laser field [49]. The dispersion of RSP with relativistic effects is given by

$$1 + \varepsilon \sqrt{\frac{n^2 - 1}{n^2 - \varepsilon}} = 0, \quad (3)$$

where $\varepsilon = 1 - \omega_p^2/\gamma_e \omega_{sp}^2$ and γ_e is the Lorentz factor of the electron. $n = ck_z/\omega_{sp} = c/v_{\text{ph}}$ with v_{ph} the phase velocity of the RSP and k_z the longitudinal component of RSP wavevector. $\varepsilon = -1$ in resonance excitation [6]. Eq. (3) can only be satisfied if $n > 1$. $n > 1$ indicates that the phase velocity of the RSP is less than c , leading to the dephasing problem. The phase velocity of the RSP with resonance condition is given as

$$v_{\text{ph}} = c\sqrt{(\varepsilon - 2)/(\varepsilon - 1)} = c\sqrt{1 - \frac{1}{\alpha}} < c, \quad (4)$$

where $\alpha = 2\gamma_e - 1$. In the non-relativistic case $\gamma_e \simeq 1$, $v_{\text{ph}} \simeq 0$, indicating that SP is a standing wave with a dominant electrostatic component [49] and is unsuitable for relativistic particle acceleration. In the ultrarelativistic case $\gamma_e \gg 1$, v_{ph} approaches c , which allows the acceleration of relativistic particles. However, when the laser strength is high enough, the wall electrons are no longer confined to the surface and can move freely to form the bubble wakefield, similar to that in a gaseous plasma [40]. The advantage of this type of bubble is that it is dephasingless since the group velocity of the laser pulse is equal to the speed of light in vacuum c .

For a Gaussian pulse propagating along the axis, the maximum γ_e is achieved at $r_L = r_t$ and then $a(r_t) = a_0 e^{-r_t^2/w_0^2}$, which suggests that the ratio r_t/w_0 also plays

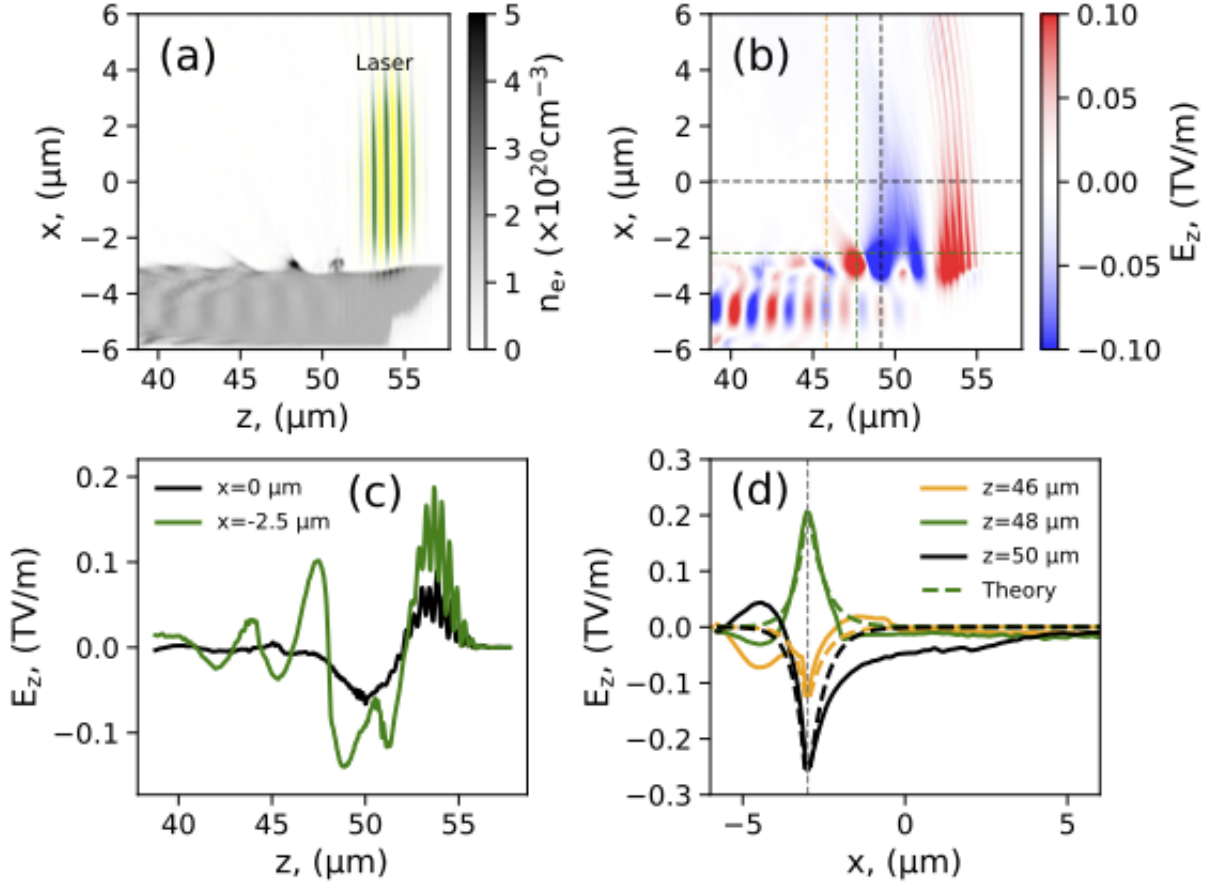


Figure 7. PIC results: SPs excitation on the flat CNT surface. (a) Density distribution of wall electrons (grey colourmap) and laser field (green-yellow colourmap). (b) Longitudinal acceleration field E_z . (c) Line plots of E_z along $x = 0 \mu\text{m}$ (black) and $x = -2.5 \mu\text{m}$ (green), indicated by the horizontal dashed lines in (b), respectively. (d) Line plots of E_z along $z = 46 \mu\text{m}$ (orange), $z = 48 \mu\text{m}$ (green) and $z = 50 \mu\text{m}$ (black), indicated by the vertical dashed lines in (b) respectively. The vertical grey line indicates the position of the interface between the CNT wall and the vacuum. The corresponding theoretical estimations are shown by the dashed lines, respectively.

a critical role in RSP excitation. The relativistic effect requires the channel radius $r_t < \omega_0 \sqrt{\ln(a_0)}$. With nanostructured CNT forests of flexible density, the RSP can be directly excited independent of laser polarisation or the matching medium. At resonance, the RSP exhibits a dominant localised electrostatic component, with its phase velocity closely matching the group velocity of the laser pulse, enabling efficient energy transfer and interaction.

We first consider a CNT forest target with a flat surface where RSP can be excited by paraxially passing a high-intensity laser pulse along z -direction, as shown in Fig. 7(a). Here, the surface is positioned at $x = -3.0 \mu\text{m}$ and extends infinitely in y and z directions, with a wall density of $n_e = 2 \times 10^{20} \text{cm}^{-3}$. The EM field with an amplitude of 0.1TV/m can leak into a small region of the surface and decay exponentially, as shown in Fig. 7(b) to (d). Theoretically, this behaviour can be explained by solving Maxwell's equations with appropriate boundary conditions at the surface [5]. The longitudinal electric

field can be expressed as

$$E_z = E_{z0} e^{-k_x x} e^{i(k_z z - \omega_{sp} t)}, \quad (5)$$

where E_{z0} is the amplitude and $k_x = \omega_{sp} \sqrt{n^2 - 1}/c$. The resonance wavelength is theoretically calculated to be $\lambda_R = 3.24 \mu\text{m}$, which agrees well with the simulation result $\lambda_{sp, PIC} \simeq 3.3 \mu\text{m}$, as shown in Fig. 7(c). RSP decays slower in vacuum than in CNTs, since $k_{x, \text{vacuum}} = \omega_{sp} \sqrt{n^2 - 1}/c < k_{x, \text{CNTs}} = \omega_{sp} \sqrt{n^2 - \epsilon}/c$ [49]. The longitudinal component E_z of the RSP along the x -direction is plotted at three different positions by solid lines in Fig. 7(d) and shows good agreement with the theoretical estimates indicated by the dashed lines. The observed deviations, e.g. at $z = 50 \mu\text{m}$ as shown by the solid and dashed black lines, are due to the influence of the laser field. With the evanescent nature of the leaky field on the flat surface, the accelerating volume is limited to a small region, e.g. $|\Delta x| < 1/k_{sp} \sim 0.2 \mu\text{m}$ for our case, making the acceleration highly sensitive to the angular distribution of both the driving and witness beams. Con-

sequently, the total charge and energy gain of the witness beam are limited.

The CNT forest can be nanostructured to include a μm -scale cylindrical vacuum channel by arranging the CNTs in an array pattern. This configuration theoretically breaks the cylindrical symmetry due to inter-tube Coulomb coupling among the periodically arranged CNTs [60], which can result in high-frequency leaky fields within the vacuum channel. However, the porous targets consist of hundreds of CNTs, with bulk dimensions significantly larger than those of a single CNT. In this case, the inter-structural interactions can be approximated as effectively uniform [40]. Consequently, mode coupling is not significant, as illustrated in Fig. 2. Without couplings between SP modes of different azimuthal indices, the leaky field can remain monochromatic, as seen in Fig. 2(a) and (b). When the intensity of the laser field is sufficiently high, these couplings become significant, potentially introducing high-frequency components into the leaky field, as shown in Fig. 5(a) and (b). Therefore, there is a compromise between the field strength and the field distribution. The quality of the leaky field, including field structure and the volume available for acceleration, can be significantly enhanced by employing a radially symmetric target, such as a hollow nanostructured CNT forest, as depicted in Fig. 1.

In a nanostructured CNT channel with a large radius r_t (e.g., $k_{sp}r_t \gg 1$), the eigenfrequencies of all SP modes become less sensitive to surface curvature and approach the resonant frequency [61, 62]. Since the length of the target is significantly larger than the channel radius ($L \gg r_t$), the electric potential of leaky RSP modes in a cylindrical channel can be derived by solving the Laplace equation in cylindrical coordinates (r, ϕ, z) as follows [37]:

$$\varphi_m(r, \phi, z, t) = \frac{\varphi_A}{I_m(k_{sp}r_t)} I_m(k_{sp}r) e^{im\phi} e^{i(k_{sp}z - \omega_{sp}t)}, \quad (6)$$

where φ_A is the amplitude and m is an integer index. The electric field can be written as $\mathbf{E} = -\nabla\varphi$. It can be seen that only the axial mode $m = 0$ does not decay to zero at any point within the vacuum channel, while the other modes decay rapidly and are zero at $r = 0$. This rapid decay renders the other modes unsuitable for efficient acceleration. The longitudinal component of the leaky field is given by

$$E_z = -\partial\varphi_0/\partial z = -ik_{sp} \frac{\varphi_A}{I_0(k_{sp}r_t)} I_0(k_{sp}r) e^{i(k_{sp}z - \omega_{sp}t)}, \quad (7)$$

which remains non-zero inside the vacuum channel. The mode $m = 0$ corresponds to a quasi-uniform leaky accelerating field with cylindrical symmetry as presented in Fig. 2 (a). The transverse component is given by

$$W_r = -\partial\varphi_0/\partial r = -k_{sp} \frac{\varphi_A}{I_0(k_{sp}r_t)} I_1(k_{sp}r) e^{i(k_{sp}z - \omega_{sp}t)}, \quad (8)$$

which decays to zero and exists only in a narrow region near the surface, in agreement with the simulation re-

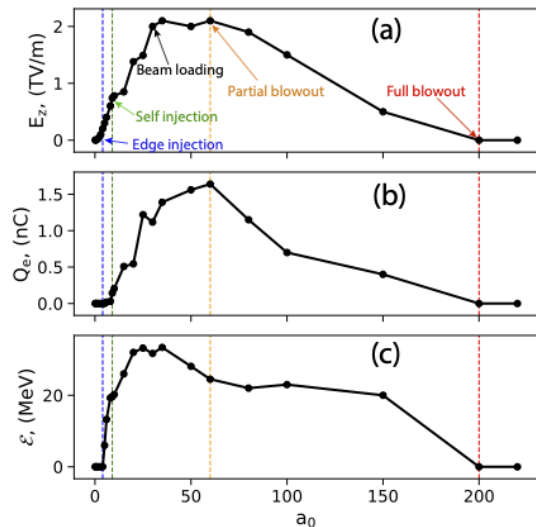


Figure 8. PIC results: Dependence of SPs excitation on normalised laser strength a_0 . (a)-(c) Peak of acceleration field E_z , total charge Q_e and mean energy \mathcal{E} of accelerated electrons after 70 μm propagation, respectively. The vertical dashed lines indicate the position where edge (blue) and self-injections (green), partial (orange) and full (red) blowouts begin.

sults shown in Fig. 2(b) and 5(b). From Eqs. (7) and (8), it can be seen that there is a $\pi/2$ phase region where either negatively or positively charged particles can experience both acceleration and focusing forces. Therefore, the leaky field of the fundamental RSP mode, $m = 0$, is suitable for accelerating both electrons and positrons.

C. Wall electron transition and cascaded leaky RSPs excitation

The key difference between the solid-state forest target and a uniform gaseous plasma is the presence of the solid inner surface, over which the electrical potential restricts the wall electrons from freely crossing the boundary. For an electron at the wall to overcome this potential barrier, it must have sufficient transverse momentum. Wall electrons gain greater momentum in stronger laser fields, increasing the probability of crossing the inner surface and becoming trapped in the leaky field. Therefore, for a specific target configuration, the parameter a_0 determines both the excitation of RSPs and the probability of wall electrons transitioning across the surface for injection.

A series of simulations were performed with a_0 values ranging from 0.1 to 220. The effects on the amplitude of the acceleration field (E_z), the total charge of the injected electron beam (Q_e), and the mean energy (\mathcal{E}) of the accelerated electron beam are presented in Fig.8 (a), (b) and (c), respectively. As a_0 increases, the RSPs become stronger, resulting in electron beams with higher

charge that can be accelerated to greater energies. Edge injection occurs for $4 < a_0 < 9$, while self-injection begins at $a_0 \geq 9$, where a significantly larger number of electrons are injected into the leaky field. At $a_0 > 30$, the beam loading effect becomes significant, reducing the effective acceleration field and energy gain rate. At low values of $a_0 < 4$, wall electrons cannot overcome the inner surface potential barrier, preventing any electron injection into the central vacuum channel. When $a_0 < 2$, SP becomes non-relativistic. Simulations also reveal critical thresholds for bubble wakefield excitation and the blowout phenomenon. In a moderately high laser pulse range ($30 < a_0 < 50$), all the wall electrons gain sufficient transverse momentum to freely cross the inner surface. These results in the formation of plasma bubbles, similar to those in uniform plasmas, but with significantly enhanced field amplitudes that exceed the coherent field limit due to the mitigation of wave breaking. As the laser strength increases further ($a_0 > 50$), wall electrons begin to acquire enough outward momentum from ponderomotive scattering to cross the outer surface of the forest target of finite wall thickness and become ejected from the target—a phenomenon referred to as the blowout effect here. In the range $50 < a_0 < 200$, partial blowout occurs where a fraction of the wall electrons are ejected from the outer wall, leading to a reduction in the acceleration field (E_z), total injected charge (Q_e), and beam energy (\mathcal{E}). Full blowout occurs at extremely high laser strengths ($a_0 > 200$), where all wall electrons are permanently ejected from the outer surface. Consequently, no sustained acceleration field is formed within the vacuum channel, and particle acceleration ceases entirely. These thresholds for a_0 depend on the balance between laser pulse intensity and target geometry, varying with different target and laser configurations. This interplay highlights the importance of precise tuning to optimise the acceleration process while avoiding undesirable blowout effects.

The robustness of RSP excitation enables efficient RSP-based acceleration in a cascading manner. This approach is highly advantageous for high-power laser-driven experiments, where both beam charge and energy can be significantly increased. Additionally, the energy spectrum of the accelerated electrons can be substantially improved. A high-intensity laser pulse can initially drive strong edge injection and self-injection. As the laser energy depletes and the laser strength (a_0) decreases, the self-injection process gradually ceases. However, the leaky field remains well-structured and stable, ensuring that the self-trapped electrons continue to be accelerated. This leads to a narrower energy spectrum for the accelerated beam. For example, a laser pulse with an initial strength of $a_0 = 30$ can trap an electron beam of charge 2.15 nC in the leaky field, which is accelerated to 180 MeV after 354 μm propagation as shown in Fig. 9. The energy spectrum has a 20% spread and can extend up to 340 MeV. This indicates an average acceleration gradient of $G_{\text{AVG}} = 0.53$ TeV/m and a peak

of $G_{\text{PEAK}} = 0.96$ TeV/m.

D. Target geometry and simulation method

Table 2. Parameters of the porous CNT target used in PIC simulations.

Layer gap, g	50 nm
Pore diameter, d	100 nm
Forest channel radius, r_t	3 μm
Filling factor, f_f	0.8
Number of layers, N	20
Wall density, n_e	2×10^{20} cm^{-3}

Fully 3D particle-in-cell (PIC) simulations were conducted using the code WarpX [51]. The schematic geometry of the CNT forest target is modelled in a porous array pattern as shown in Fig. 1 (a). The transverse layout of the target design is shown in Fig. 1 (b), where the pore distribution is initialised as concentric virtual layers around the central axis. Each layer is characterised by its pore diameter d , volume filling factor f_f —representing the fraction of the layer occupied by pores—and the gap g between adjacent layers. The forest wall is modelled using an effective density n_e representation rather than resolving individual CNTs illustrated in Fig. 1(c) and (d). This approximation is justified by the immense number of densely packed CNTs in the forest and the fact that the nm-scale inner structure of individual CNT is negligible for the μm -scale dynamics in a strong field [40, 63, 64]. These targets can be fabricated using techniques such as the CVD method [43, 44] or the anodic aluminium oxide (AAO) template method. The AAO technique, in particular, offers exceptional tunability by enabling precise control over the pore structure of the template [65]. The length of the CNT forest can extend up to 10–20 mm [44], which is sufficient to meet the experimental requirements. Unless stated otherwise, the general parameters for the CNT target are summarised in Table. 2.

Vacuum sections of 20 μm and 10 μm are placed longitudinally at the head and tail of the forest target, respectively, for laser initialisation and electron beam diagnostics. The target species consists of carbon atoms, which can only be singly ionised to produce C^+ ions. Field ionisation is implemented using the Ammosov-Delone-Krainov (ADK) method [66]. The dimensions of the moving window are 12 $\mu\text{m} \times 12 \mu\text{m} \times 20 \mu\text{m}$, comprising $384 \times 384 \times 512$ cells in the x , y , and z directions, respectively. This configuration provides 3 points within each forest pore transversely, ensuring an accurate spatial representation of the structure. Each cell contains 8 macro particles, which is sufficient to solve the electron dynamics effectively. For particle and field updates, the simulations utilise the Boris pusher [67] and the CKC Maxwell solver [68].

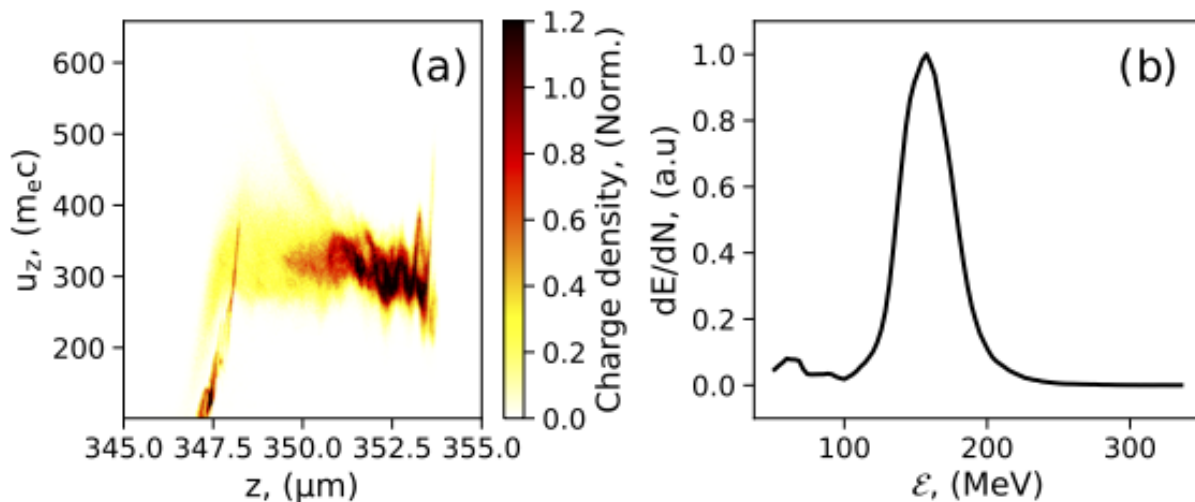


Figure 9. PIC Results: (a) Phase space and (b) energy spectrum of an electron beam self-injected and accelerated in a $354 \mu\text{m}$ -long CNT forest target. The laser and target parameters are identical to those in Fig. 5, except for an initial $a_0 = 30$.

V. CONCLUSION AND SUMMARY

In this paper, we demonstrated that a TW optical laser pulse can effectively drive the excitation of strong RSPs on the μm -scale cylindrical surface of a CNT forest. These RSPs feature an electromagnetic (EM) component that leaks into the central vacuum channel, providing acceleration fields on the order of TV/m. These fields are suitable for accelerating both relativistic negatively and positively charged particles. We propose two distinct electron injection schemes, each with unique features that enhance the experimental feasibility of this approach, paving the way for practical implementations. We also analyzed the fundamental physical principles that enable this mechanism to function. It requires the CNT forest to be in a quantum-degenerate and correlated state, a condition that is achievable under standard experimental setups. This provides a solid theoretical foundation for the feasibility of the proposed approach.

In line with recent advances in both laser-driven solid-state and plasma-based accelerators, this paper presents a novel concept for accelerating both positively and negatively charged particles by exciting a new class of SP modes, RSPs, through the ponderomotive scattering of a high-intensity optical laser pulse passing paraxially through a nanostructured CNT forest. Compared to conventional conductive materials, such as metals and semiconductors, CNTs can offer significantly higher plasmon gain due to their unique electronic structure and exceptional field confinement. This enables stronger light-matter interactions, which can substantially improve energy efficiency in experimental setups. Unlike traditional solid-state accelerators, such as crystal-based accelerators or dielectric laser accelerators (DLAs), the CNT-based accelerator leverages plasma dynamics, promising exceptionally high acceleration gradients of up to hun-

dreds of TV/m in principle. This approach can generate lepton beams in the MeV-level on μm scales or PeV-level on meter scales, offering immense potential for future high-energy applications. In contrast to gaseous plasma-based accelerators, the CNT-based method is solid-state, capable of providing much higher acceleration fields with enhanced mechanical stability, making it a promising alternative for next-generation acceleration technologies.

The experiments can be designed with the laser facilities of TW to PW power with μm -scale beam size [69]. Recent advances in modern nanofabrication techniques have enabled the production of nanostructured CNT forests with specifications that can meet the experimental requirements [70]. This unique combination makes CNT-based particle accelerators a promising solution for pushing the energy frontier in scientific discovery and also poised to significantly enhance our precision in manipulating matter for potential applications in cutting-edge fields like high-energy plasmonics, ion channeling and radiation generation.

ACKNOWLEDGEMENTS

Javier Resta-López acknowledges support by the Generalitat Valenciana under grant agreement CIDE-GENT/2019/058. This work made use of the facilities of the N8 Centre of Excellence in Computationally Intensive Research (N8 CIR) provided and funded by the N8 research partnership and EPSRC (Grant No. EP/T022167/1). The Centre is coordinated by the Universities of Durham, Manchester and York.

DATA AVAILABILITY

The datasets used and/or analysed during the current study available from the corresponding author on reasonable request.

AUTHOR CONTRIBUTIONS

All authors conceived the numerical simulations and discussed the results. B.F.L. run the simulations, processed the data and wrote the manuscript. C.W. provided the computational resources. All authors reviewed and edited the manuscript.

ADDITIONAL INFORMATION

The authors declare no competing interests.

-
- [1] D. Pines, A collective description of electron interactions: Iv. electron interaction in metals, *Phys. Rev.* **92**, 626 (1953).
- [2] D. Pines, Collective energy losses in solids, *Rev. Mod. Phys.* **28**, 184 (1956).
- [3] C. J. Powell and J. B. Swan, Origin of the characteristic electron energy losses in aluminum, *Phys. Rev.* **115**, 869 (1959).
- [4] E. A. Stern and R. A. Ferrell, Surface plasma oscillations of a degenerate electron gas, *Phys. Rev.* **120**, 130 (1960).
- [5] J. M. Pitarke, V. M. Silkin, E. V. Chulkov, and P. M. Echenique, Theory of surface plasmons and surface-plasmon polaritons, *Reports on Progress in Physics* **70**, 1 (2007).
- [6] R. H. Ritchie, Plasma losses by fast electrons in thin films, *Phys. Rev.* **106**, 874 (1957).
- [7] J. E. Inglesfield and E. Wikborg, The van der waals interaction between metals, *Journal of Physics F: Metal Physics* **5**, 1475 (1975).
- [8] R. H. Ritchie, Surface plasmons and the image force in metals, *Physics Letters A* **38**, 189 (1972).
- [9] W. Knoll, Interfaces and thin films as seen by bound electromagnetic waves, *Annual Review of Physical Chemistry* **49**, 569 (1998).
- [10] G. I. Janith, H. S. Herath, N. Hendeniya, D. Attygalle, D. A. S. Amarasinghe, V. Logeeshan, P. M. T. B. Wickramasinghe, and Y. S. Wijayasinghe, Advances in surface plasmon resonance biosensors for medical diagnostics: An overview of recent developments and techniques, *Journal of Pharmaceutical and Biomedical Analysis Open* **2**, 100019 (2023).
- [11] E. Ozbay, Plasmonics: Merging photonics and electronics at nanoscale dimensions, *Science* **311**, 189 (2006).
- [12] R. Berndt, J. K. Gimzewski, and P. Johansson, Inelastic tunneling excitation of tip-induced plasmon modes on noble-metal surfaces, *Phys. Rev. Lett.* **67**, 3796 (1991).
- [13] G. Flätgen, K. Krischer, B. Pettinger, K. Doblhofer, H. Junkes, and G. Ertl, Two-dimensional imaging of potential waves in electrochemical systems by surface plasmon microscopy, *Science* **269**, 668 (1995).
- [14] S. E. Irvine, A. Dechant, and A. Y. Elezzabi, Generation of 0.4-keV femtosecond electron pulses using impulsively excited surface plasmons, *Phys. Rev. Lett.* **93**, 184801 (2004).
- [15] L. Wang and K. Yin, Ultra-compact plasmonic electron accelerator on chip, *Results in Physics* **35**, 105355 (2022).
- [16] G.-y. Hu, A.-l. Lei, W.-t. Wang, X. Wang, L.-g. Huang, J.-w. Wang, Y. Xu, J.-s. Liu, W. Yu, B.-f. Shen, R.-x. Li, and Z.-z. Xu, Collimated hot electron jets generated from subwavelength grating targets irradiated by intense short-pulse laser, *Physics of Plasmas* **17**, 033109 (2010).
- [17] S. Bagchi, P. Prem Kiran, W. M. Wang, Z. M. Sheng, M. K. Bhuyan, M. Krishnamurthy, and G. Ravindra Kumar, Surface-plasmon-enhanced MeV ions from femtosecond laser irradiated, periodically modulated surfaces, *Physics of Plasmas* **19**, 030703 (2012).
- [18] M. Cerchez, A. L. Giesecke, C. Peth, M. Toncian, B. Albertazzi, J. Fuchs, O. Willi, and T. Toncian, Generation of laser-driven higher harmonics from grating targets, *Phys. Rev. Lett.* **110**, 065003 (2013).
- [19] M. A. Purvis, V. N. Shlyaptsev, R. Hollinger, C. Bargsten, A. Pukhov, A. Prieto, Y. Wang, B. M. Luther, L. Yin, S. Wang, and J. J. Rocca, Relativistic plasma nanophotonics for ultrahigh energy density physics, *Nature Photonics* **7**, 796 (2013).
- [20] T. Ceccotti, V. Floquet, A. Sgattoni, A. Bigongiari, O. Klimo, M. Raynaud, C. Riconda, A. Heron, F. Baffigi, L. Labate, L. A. Gizzi, L. Vassura, J. Fuchs, M. Passoni, M. Květon, F. Novotny, M. Possolt, J. Prokūpek, J. Proška, J. Pšikal, L. Štolcová, A. Velyhan, M. Bougeard, P. D'Oliveira, O. Tcherbakoff, F. Réau, P. Martin, and A. Macchi, Evidence of resonant surface-wave excitation in the relativistic regime through measurements of proton acceleration from grating targets, *Phys. Rev. Lett.* **111**, 185001 (2013).
- [21] L. Fedeli, A. Sgattoni, G. Cantonio, D. Garzella, F. Réau, I. Prencipe, M. Passoni, M. Raynaud, M. Květon, J. Proška, A. Macchi, and T. Ceccotti, Electron acceleration by relativistic surface plasmons in laser-grating interaction, *Phys. Rev. Lett.* **116**, 015001 (2016).
- [22] G. Cantonio, A. Sgattoni, L. Fedeli, D. Garzella, F. Réau, C. Riconda, A. Macchi, and T. Ceccotti, Extensive study of electron acceleration by relativistic surface plasmons, *Physics of Plasmas* **25**, 031907 (2018).
- [23] X. M. Zhu, R. Prasad, M. Swantusch, B. Aurand, A. A. Andreev, O. Willi, and M. Cerchez, Relativistic electron acceleration by surface plasma waves excited with high intensity laser pulses, *High Power Laser Science and Engineering* **8**, e15 (2020).
- [24] D. an der Brügge, N. Kumar, A. Pukhov, and C. Rödel, Influence of surface waves on plasma high-order harmonic generation, *Phys. Rev. Lett.* **108**, 125002 (2012).

- [25] J. Pendry, Playing tricks with light, *Science* **285**, 1687 (1999).
- [26] E. Prodan, C. Radloff, N. J. Halas, and P. Nordlander, A hybridization model for the plasmon response of complex nanostructures, *Science* **302**, 419 (2003).
- [27] J. Zhang and L. Zhang, Nanostructures for surface plasmons, *Advances in Optics and Photonics* **4**, 157 (2012).
- [28] Editorial, Surface plasmon resurrection (editorial), *Nature Photonics* **6**, 707 (2012).
- [29] A. Sgattoni, L. Fedeli, G. Cantono, T. Ceccotti, and A. Macchi, High field plasmonics and laser-plasma acceleration in solid targets, *Plasma Physics and Controlled Fusion* **58**, 014004 (2016).
- [30] D. E. Cardenas, T. M. Ostermayr, L. Di Lucchio, L. Hofmann, M. F. Kling, P. Gibbon, J. Schreiber, and L. Veisz, Sub-cycle dynamics in relativistic nanoplasma acceleration, *Scientific Reports* **9**, 7321 (2019).
- [31] J. Sarma, A. McIlvenny, N. Das, M. Borghesi, and A. Macchi, Surface plasmon-driven electron and proton acceleration without grating coupling, *New Journal of Physics* **24**, 073023 (2022).
- [32] Y. Arikawa, A. Morace, Y. Abe, N. Iwata, Y. Sentoku, A. Yogo, K. Matsuo, M. Nakai, H. Nagatomo, K. Mima, H. Nishimura, S. Fujioka, R. Kodama, S. Inoue, M. Hashida, S. Sakabe, D. De Luis, G. Gatti, M. Huault, J. Pérez-Hernández, L. Roso, and L. Volpe, Demonstration of efficient relativistic electron acceleration by surface plasmonics with sequential target processing using high repetition lasers, *Physical Review Research* **5**, 013062 (2023).
- [33] A. Eatemadi, H. Daraee, H. Karimkhanloo, M. Kouhi, N. Zarghami, A. Akbarzadeh, M. Abasi, Y. Hanifehpour, and S. W. Joo, Carbon nanotubes: properties, synthesis, purification, and medical applications, *Nanoscale Research Letters* **9**, 393 (2014).
- [34] S. Rathinavel, K. Priyadharshini, and D. Panda, A review on carbon nanotube: An overview of synthesis, properties, functionalization, characterization, and the application, *Materials Science and Engineering: B* **268**, 115095 (2021).
- [35] J. E. Fischer and A. T. Johnson, Electronic properties of carbon nanotubes, *Current Opinion in Solid State and Materials Science* **4**, 28 (1999).
- [36] T. Ando, The electronic properties of graphene and carbon nanotubes, *NPG Asia Materials* **1**, 17 (2009).
- [37] M. Schmeits, Surface plasmon excitation on cylindrical surfaces, *Solid State Communications* **67**, 169 (1988).
- [38] S. Frank, P. Poncharal, Z. L. Wang, and W. A. d. Heer, Carbon nanotube quantum resistors, *Science* **280**, 1744 (1998).
- [39] P. Poncharal, C. Berger, Y. Yi, Z. L. Wang, and W. A. de Heer, Room temperature ballistic conduction in carbon nanotubes, *The Journal of Physical Chemistry B* **106**, 12104 (2002).
- [40] A. Bonatto, G. Xia, O. Apsimon, C. Bontoiu, E. Kukstas, V. Rodin, M. Yadav, C. P. Welsch, and J. Resta-López, Exploring ultra-high-intensity wakefields in carbon nanotube arrays: An effective plasma-density approach, *Physics of Plasmas* **30**, 033105 (2023).
- [41] J. Li, C. Papadopoulos, J. M. Xu, and M. Moskovits, Highly-ordered carbon nanotube arrays for electronics applications, *Applied Physics Letters* **75**, 367 (1999).
- [42] F. Sarasini, J. Tirillò, M. Lilli, M. P. Bracciale, P. E. Vulum, F. Berto, G. De Bellis, A. Tamburrano, G. Cavoto, F. Pandolfi, and I. Rago, Highly aligned growth of carbon nanotube forests with in-situ catalyst generation: A route to multifunctional basalt fibres, *Composites Part B: Engineering* **243**, 110136 (2022).
- [43] J. Robertson, G. Zhong, S. Esconjauregui, C. Zhang, M. Fouquet, and S. Hofmann, Chemical vapor deposition of carbon nanotube forests, *physica status solidi (b)* **249**, 2315 (2012).
- [44] H. Sugime, T. Sato, R. Nakagawa, T. Hayashi, Y. Inoue, and S. Noda, Ultra-long carbon nanotube forest via in situ supplements of iron and aluminum vapor sources, *Carbon* **172**, 772 (2021).
- [45] D. N. Futaba, K. Hata, T. Namai, T. Yamada, K. Mizuno, Y. Hayamizu, M. Yumura, and S. Iijima, 84% catalyst activity of water-assisted growth of single walled carbon nanotube forest characterization by a statistical and macroscopic approach, *The Journal of Physical Chemistry B* **110**, 8035 (2006).
- [46] S. Iijima, Helical microtubules of graphitic carbon, *Nature* **354**, 56 (1991).
- [47] W. Yang, X.-G. Zheng, S.-G. Wang, and H.-J. Jin, Nanoporous aluminum by galvanic replacement: Dealloying and inward-growth plating, *Journal of The Electrochemical Society* **165**, C492 (2018).
- [48] M. Yu, H. H. Funke, J. L. Falconer, and R. D. Noble, High density, vertically-aligned carbon nanotube membranes, *Nano Letters* **9**, 225 (2009).
- [49] R. Dragila and S. Vukovic, Excitation of surface waves by an electromagnetic wave packet, *Physical Review Letters* **61**, 2759 (1988).
- [50] E. Kretschmann and H. Raether, Notizen: Radiative decay of non radiative surface plasmons excited by light, *J. High Energy Phys.* **23** (12), 2135.
- [51] *SC22: International Conference for High Performance Computing, Networking, Storage and Analysis* (2022).
- [52] E. H. Hwang and S. Das Sarma, Dielectric function, screening, and plasmons in two-dimensional graphene, *Phys. Rev. B* **75**, 205418 (2007).
- [53] H. Yan, T. Low, W. Zhu, Y. Wu, M. Freitag, X. Li, F. Guinea, P. Avouris, and F. Xia, Damping pathways of mid-infrared plasmons in graphene nanostructures, *Nature Photonics* **7**, 394 (2013).
- [54] I. Chaikovska, R. Chehab, V. Kubyskyi, S. Ogur, A. Ushakov, A. Variola, P. Sievers, P. Musumeci, L. Bandiera, Y. Enomoto, M. J. Hogan, and P. Martyshkin, Positron sources: from conventional to advanced accelerator concepts-based colliders, *Journal of Instrumentation* **17** (05), P05015.
- [55] C. Bontoiu, Ö. Apsimon, E. Kukstas, V. Rodin, M. Yadav, C. Welsch, J. Resta-López, A. Bonatto, and G. Xia, TeV/m catapult acceleration of electrons in graphene layers, *Scientific Reports* **13**, 1330 (2023).
- [56] Y. Morimoto, Attosecond electron-beam technology: a review of recent progress, *Microscopy* **72**, 2 (2023).
- [57] A. Sommerfeld, Zur elektronentheorie der metalle auf grund der fermischen statistik, *Zeitschrift für Physik* **47**, 1 (1928).
- [58] N. W. Ashcroft and N. D. Mermin, *Solid state physics* (Holt, Rinehart and Winston, New York, NY, 1976).
- [59] M. Bockrath, D. H. Cobden, J. Lu, A. G. Rinzler, R. E. Smalley, L. Balents, and P. L. McEuen, Luttinger-liquid behaviour in carbon nanotubes, *Nature* **397**, 598 (1999).

- [60] M. F. Lin, F. L. Shyu, and R. B. Chen, Dielectric response of an electron-gas nanotube superlattice, *Physics Letters A* **253**, 88 (1999).
- [61] M. Schmeits, Surface-plasmon coupling in cylindrical pores, *Phys. Rev. B* **39**, 7567 (1989).
- [62] R. J. Warmack, R. S. Becker, V. E. Anderson, R. H. Ritchie, Y. T. Chu, J. Little, and T. L. Ferrell, Surface-plasmon excitation during aloof scattering of low-energy electrons in micropores in a thin metal foil, *Phys. Rev. B* **29**, 4375 (1984).
- [63] R. Englman and R. Ruppin, Optical lattice vibrations in finite ionic crystals: I, *Journal of Physics C: Solid State Physics* **1**, 614 (1968).
- [64] S. Hakimi, T. Nguyen, D. Farinella, C. K. Lau, H.-Y. Wang, P. Taborek, F. Dollar, and T. Tajima, Wakefield in solid state plasma with the ionic lattice force, *Physics of Plasmas* **25**, 023112 (2018).
- [65] P. Hou, C. Liu, C. Shi, and H. Cheng, Carbon nanotubes prepared by anodic aluminum oxide template method, *Chinese Science Bulletin* **57**, 187 (2012).
- [66] M. V. Ammosov, N. B. Delone, and V. P. Krainov, *Tunnel ionization of complex atoms and atomic ions in electromagnetic field* (SPIE Society of Photo-Optical Instrumentation Engineers, United States, 1986).
- [67] J. P. Boris, Relativistic plasma simulation-optimization of a hybrid code, *Proceeding of Fourth Conference on Numerical Simulations of Plasmas* (1970).
- [68] B. M. Cowan, D. L. Bruhwiler, J. R. Cary, E. Cormier-Michel, and C. G. R. Geddes, Generalized algorithm for control of numerical dispersion in explicit time-domain electromagnetic simulations, *Phys. Rev. ST Accel. Beams* **16**, 041303 (2013).
- [69] G. Mourou, Nobel lecture: Extreme light physics and application, *Rev. Mod. Phys.* **91**, 030501 (2019).
- [70] K. Wang, F. Wang, Q. Jiang, P. Zhu, K. Leu, and R. Zhang, Controlled synthesis, properties, and applications of ultralong carbon nanotubes, *Nanoscale Advances* **6**, 4504 (2024).